JOURNAL OF PETROLOGY | VOLUME 52 | NUMBER 5 | PAGES 839–856 | 2011 | doi:10.1093/petrology/egr004

Electron Backscatter Diffraction (EBSD) Analysis of Bassanite Transformation Textures and Crystal Structure Produced from Experimentally Deformed and Dehydrated Gypsum

REBECCA C. HILDYARD*, SERGIO LLANA-FÚNEZ†, JOHN WHEELER, DANIEL R. FAULKNER AND DAVID J. PRIOR

DEPARTMENT OF EARTH AND OCEAN SCIENCES, UNIVERSITY OF LIVERPOOL, 4 BROWNLOW STREET, LIVERPOOL L69 3GP, UK

RECEIVED APRIL 12, 2010; ACCEPTED JANUARY 25, 2011
ADVANCE ACCESS PUBLICATION FEBRUARY 27, 2011

Dehydration reactions have important effects on fluid flow, pore pressure and brittle failure in the Earth. The rates and mechanisms of reaction are relevant to understanding those effects. The microstructures of a set of samples containing bassanite and gypsum from dehydration experiments on Volterra gypsum have been analysed by conventional transmitted light microscopy and electron backscatter diffraction (EBSD). These techniques have been used to characterize the varying crystal morphology and to measure the crystallographic preferred orientation (CPO) of the samples. In some samples bassanite grains show two distinct morphologies; large (0·5–2 mm), euhedral crystals and small (<50 μm), acicular crystals: these represent the two different bassanite crystal habits. Bassanite was indexed using EBSD for the first time, and problems related to significant mis-indexing resulting from the pseudotrigonal symmetry of bassanite are resolved. The original starting material has a strong, local and measurable CPO. A strong CPO in post-experiment bassanite is found to mimic the original gypsum c-axis orientation. Bassanite grain size is related to the degree of reaction overstep. Spatial heterogeneity in bassanite distribution may indicate the development of fluid pathways within the samples.

KEY WORDS: *EBSD; gypsum; bassanite; mis-indexing; crystallography; CPO*

INTRODUCTION

Dehydration reactions are common in the Earth. The fluid released may transport dissolved chemicals and hydrate minerals along the fluid pathways. The fluid pressure is controlled by reaction rate and permeability; if high the fluid pressure can trigger brittle failure (Raleigh & Paterson, 1965, 1966; Murrell & Ismail, 1976; Olgaard *et al.*, 1995; Miller *et al.*, 2003). These are bulk phenomena and it is important, then, to understand the controls on reaction rate during dehydration. It is expected that a high degree of overstepping will lead to a fast reaction rate and finer-grained reaction products (Yardley, 1989; Lasaga, 1998) but this has rarely been explored systematically in experiments. Rates and mechanisms of reaction may also be influenced by the crystallography of the reactant phases. However, the crystallography of dehydration reactants and products is again rarely documented.

Gypsum dehydrates to bassanite at relatively low temperatures (~105°C at 40 MPa total pressure (McConnell *et al.*, 1987) and thus the reaction is readily accessible at laboratory experimental conditions. Dehydration of gypsum to bassanite has effects on pore pressure and thus the strength of a rock (e.g. Hubbert & Rubey, 1959; Heard & Rubey, 1966; Murrell & Ismail, 1976;

---

*Corresponding author. Telephone: +44 151 794 5202. Fax: +44 151 794 5169. E-mail: rebecca.hildyard101@btinternet.com
†Present address: Departamento de Geología, Universidad de Oviedo, calle Arias de Velasco s/n, 33005 Oviedo, Spain.

Olgaard *et al.*, 1995). Knowledge of the microstructures and crystallographic textures resulting from dehydration of gypsum under experimental conditions is therefore important.

The present study aims to characterize the macroscopic distribution, microstructure and texture of the reaction products of dehydration experiments conducted on gypsum using a range of pre-existing experimental samples. Measured crystallographic preferred orientation (CPO) in gypsum (both the original starting material and the post-experimented material) and bassanite are compared to establish the degree to which bassanite inherits any pre-existing texture. Attempts have also been made to characterize the varying crystal morphology of bassanite within the experimental samples. For the first time, electron backscatter diffraction (EBSD) is used as a technique to investigate the microstructures and crystallographic preferred orientation in bassanite. One of the major outcomes of this work is a description of the non-trivial steps taken to overcome substantial mis-indexing problems associated with EBSD of bassanite, and as such these are discussed in the results section rather than the methods section.

Bassanite—crystallography and formation

In the calcium sulphate system $CaSO_4 \cdot xH_2O$ (where $0 \leq x \leq 2$) a number of crystalline phases occur related to the amount of H_2O; these are gypsum ($x = 2$); the hemi-hydrates α-bassanite (α-$CaSO_4.0{\cdot}5H_2O$) and β-bassanite (β-$CaSO_4.0{\cdot}5H_2O$) and the soluble (γ-$CaSO_4$) and insoluble ($CaSO_4$) forms of anhydrite. There have also been further high-pressure, >4 GPa, anhydrous phases documented, which are not discussed here (e.g. see Chen *et al.*, 2001). Gypsum is monoclinic (Pedersen & Semmingsen, 1982; Schofield *et al.*, 1996; Boeyens & Ichharam 2002; also see Table 1) whereas the crystal structure of bassanite is described as either trigonal, or monoclinic but pseudotrigonal (Table 1). 'Pseudotrigonal' means that the monoclinic unit cell has angles and axes that are close to those of a trigonal phase (e.g. Ballirano *et al.*, 2001, fig. 3).

A number of researchers have identified the space group of bassanite as I2 (Table 1). In what follows, however, we have needed to transform the atomic positions into space group C2. This is because the Channel5 software used for the EBSD analysis discussed below does not include space group I2. Recalculation of the atomic positions for a redefined unit cell was done via a transformation matrix in a routine made available by the Bilbao Crystallographic Server (Aroyo *et al.*, 2006*a*, 2006*b*). A similar transformation process was necessary for the successful indexing of orthorhombic anhydrite (Hildyard *et al.*, 2009*a*) and monoclinic gypsum (Hildyard *et al.*, 2009*b*). In the C2 setting, the I2 crystal axes become transformed so that the new *a*-axis is the old $-a-c$, and the new *c*-axis is the old *a*-axis. If (x_{C2}, y_{C2}, z_{C2}) are the coordinates of a lattice vector in the C2 setting (similar notation for I2) then

$$(x_{C2}, y_{C2}, z_{C2}) = (-z_{I2}, y_{I2}, x_{I2} - z_{I2})$$

and conversely

$$(x_{I2}, y_{I2}, z_{I2}) = (z_{C2} - x_{C2}, y_{C2}, -x_{C2}).$$

It is important to note that in this contribution, the C2 setting is used and that all Weber indices have different meaning from those in the I2 setting. Specifically, the '*c*-axis' or ⟨001⟩ axis in the I2 setting becomes the ⟨101⟩ axis in the C2 setting. For this reason the use of the term '*c*-axis' in relation to bassanite studied here is avoided (unless the setting is explicitly stated), as its meaning depends on which setting is in use. Weber indices are used to indicate bassanite crystal directions, with the C2 setting assumed unless stated otherwise. The most successful EBSD indexing was achieved using atomic positions (transformed from I2 to C2, Table 4) from Ballirano *et al.* (2001), rather than those from Bezou *et al.* (1995) as used by Hildyard *et al.* (2009*a*). The ⟨001⟩ axis in the I2 setting (i.e. the ⟨101⟩ axis in the C2 setting) corresponds to the three-fold pseudotrigonal symmetry axis. It should be noted that the change from the I2 to C2 setting does not in any sense revise the atomic positions, or influence the reflector intensities that the Channel5 software calculates from those positions; it is done simply because Channel5 does not implement the I2 setting.

The two forms of bassanite (α and β) are not thermodynamically stable at normal atmospheric conditions (1 atm pressure and ~17°C) and each of the two types documented in the literature is formed by different processes. The general consensus is that α-bassanite is a metastable phase prepared from dehydration of gypsum in an acidic aqueous suspension and β-bassanite is prepared by 'drying' at high temperatures in dry air or a vacuum (e.g. Bezou *et al.*, 1995; Singh & Middendorf, 2007; Christensen *et al.*, 2008). The dehydration of a gypsum single crystal to α-bassanite is said to be a topotactic solid-state reaction that takes place with the retention of the crystallographic *c*-axis (in a monoclinic setting), but dehydration of a gypsum aggregate results in growth and nucleation of α-bassanite on parent gypsum without directional correlation (Freyer & Voigt, 2003). α-Bassanite has been shown to crystallize as aggregates of hexagonal, idiomorphic crystals with sharp crystal edges (Follner *et al.*, 2002; Freyer & Voigt, 2003; Singh & Middendorf, 2007). Similarly, the dehydration of gypsum to β-bassanite (trigonal) is also said to be topotactic with the original [010] or [001] axis of gypsum becoming the new [001] axis in bassanite (Freyer & Voigt, 2003). β-bassanite is said to form as flaky particles or small crystal fibres, which in some studies are pseudomorphs after gypsum (Singh & Middendorf, 2007). Follner *et al.* (2002) suggested that during dehydration of

Table 1: Crystallographic data for gypsum, bassanite and anhydrite (after Christensen et al.*, 2008)*

Type	Unit cell parameters						Space group	Crystal system	Ref.
	a	*B*	*c*	α	β	γ			
Gypsum									
$CaSO_4.H_2O$	5·679	15·202	6·522	90	118·43	90	I2/a	Mono	1
	5·674	15·105	6·491	90	118·513	90	I2/a	Mono	2
	6·284	15·200	6·523	90	127·41	90	C2/c	Mono	3
Hemihydrates									
α-$CaSO_4.0{\cdot}5H_2O$	11·94	6·83	12·70	90	90·6	90	C121	Mono	4
α-$CaSO_4.0{\cdot}67H_2O$	12·028	6·927	12·67	90	90·21	90	I2	Mono	5
α-$CaSO_4.0{\cdot}53H_2O$	12·028	6·931	12·692	90	90·18	90	I2	Mono	6
α-$CaSO_4.0{\cdot}5H_2O$	12·032	6·927	12·671	90	90·27	90	I121	Mono	7
α-$CaSO_4.0{\cdot}5H_2O$	12·035	6·929	12·67	90	90·27	90	I2	Mono	8
β-$CaSO_4.0{\cdot}5H_2O$	6·937	6·937	6·345	90	90	120	$P3_121$	Trig	9
β-$CaSO_4.0{\cdot}5H_2O$	6·931	6·931	12·736	90	90	120	$P3_1$	Trig	16
β-$CaSO_4.0{\cdot}8H_2O$	6·968	6·968	6·410	90	90	120	$P3_121$	Trig	10
β-$CaSO_4.0{\cdot}62H_2O$	13·861	13·861	12·739	90	90	120		Trig	6
β-$CaSO_4.0{\cdot}6H_2O$	11·984	6·929	12·750	90	90	90	I121	Mono	7
Anhydrite (soluble)									
γ-$CaSO_4$	6·982	6·982	6·340	90	90	120	$P6_222$	Hex	11
γ-$CaSO_4$	6·969	6·969	6·303	90	90	120	$P6_222$	Hex	12
γ-$CaSO_4$	12·077	6·972	6·304	90	90	90	C222	Ortho	7
Anhydrite (insoluble)									
$CaSO_4$	6·991	6·996	6·238	90	90	90	Amma	Ortho	13
$CaSO_4$	6·993	6·995	6·245	90	90	90	Amma	Ortho	14
$CaSO_4$	7·006	6·998	6·245	90	90	90	Amma	Ortho	15

1, Pederson & Semmingsen (1982); 2, Schofield *et al*. (1996); 3, Boeyens & Ichharam (2002); 4, Gallitelli (1933); 5, Bushuev & Borisov (1982); 6, Kuzel & Hauner (1987); 7, Bezou *et al*. (1995); 8, Ballirano *et al*. (2001); 9, Abriel & Nesper (1993); 10, Abriel (1983); 11, Florke (1952); 12, Lager *et al*. (1984); 13, Cheng & Zussman (1963); 14, Hawthorne & Ferguson (1975); 15, Kirfel & Will (1980); 16, Christensen *et al*. (2008).

gypsum, bassanite grows heteroepitaxially on gypsum and the (100) faces in trigonal bassanite run parallel, for the most part, with the (010) faces in gypsum.

METHODS

Experimental approach

Triaxial deformation rig

All dehydration, hydrostatic (where $\sigma_1 = \sigma_2 = \sigma_3$) compaction and deformation experiments were run in a triaxial ($\sigma_1 > \sigma_2 = \sigma_3 > 0$) deformation apparatus located, designed and built at the Rock Deformation Laboratory in the University of Liverpool (Mitchell & Faulkner, 2008; Llana-Funez *et al*., in preparation). The rig uses low-viscosity silicon oil as a confining medium and distilled water as pore fluid. Pressure can be measured with a resolution better than 50 Pa and a pore fluid volumometer can measure volumes change of $\geq 01\,mm^3$. The pressure vessel is heated externally and the temperature in the sample is measured by a thermocouple, which is hosted in the upper part of the sample assembly (Fig. 1). The temperature gradient along the specimen length (50 mm long) is less than 2°C. Cylindrical specimen cores of 20 mm diameter and various lengths were obtained from three blocks of Volterra gypsum (Fig. 2), similar to those used by previous workers (Ko *et al*., 1995; Olgaard *et al*., 1995; Stretton, 1996; Wong *et al*., 1997). Cores were squared and inserted in annealed copper jackets that isolate the pore fluid from the confining fluid. The seal was achieved using Viton O-rings.

Experimental procedure during dehydration

Once jacketed and inside the deformation apparatus, the Volterra gypsum specimens were initially pressurized to relatively high confining and fluid pressure before heating

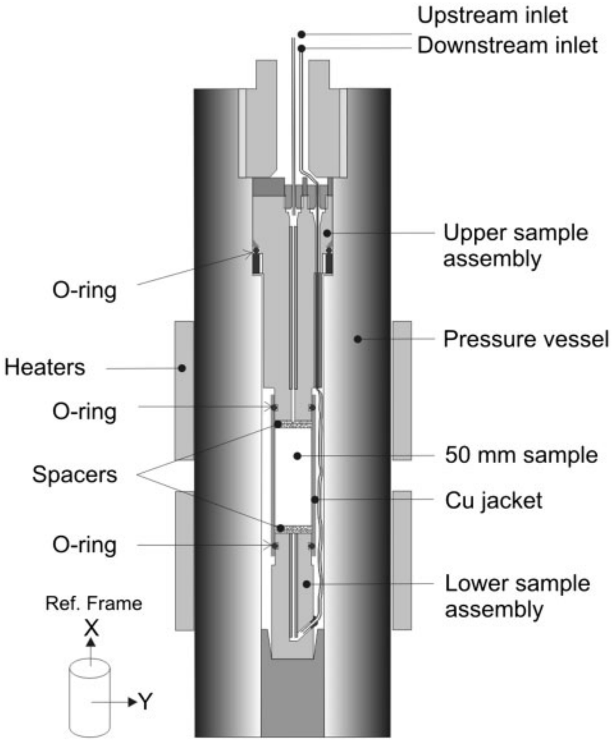

Fig. 1. Schematic diagram of the experimental apparatus, modified after Mitchell (2007) to show the location of the heaters.

to the specified starting temperature for that experiment. This was done to suppress the reaction while initial and steady temperature values were reached. A brief outline of the three types of experiment is given below and further specific experimental conditions are given in Table 2.

Dehydration under low effective pressure. Samples GYP37, GYP38 and GYP43 were dehydrated at temperatures between 110 and 125°C and low effective pressure (4–10 MPa) for durations ranging from 1 to 5 days. Low effective pressures minimized compaction and maximized the preservation of the pore space. Assuming no compaction, the complete conversion of gypsum to bassanite implies around 8–9% of water expulsion. Table 2 therefore indicates that the degree of reaction was variable between experiments, and this is confirmed by the presence of gypsum in some of the thin sections of post-experiment material.

Dehydration under low effective pressure then post-dehydration compaction. Samples GYP30 and GYP3334 were first dehydrated and subsequently compacted. During the first stage of the experiments the samples were dehydrated at low effective pressures (2–5 MPa) at temperatures between 115 and 140°C. During this stage between 3 and 8% pore fluid was expelled. In the second stage the samples were cooled to between 30 and 50°C and then subject to incremental confining pressure increases to compact the samples. During this second stage further pore fluid was expelled from the samples. This was done to identify the compaction characteristics of the porous aggregate, the results of which will be reported elsewhere.

Dehydration under high effective pressure (simultaneous compaction). Samples GYP56 and GYP57 were dehydrated at high effective pressure such that they were simultaneously compacted as the dehydration reaction progressed. First both samples were dehydrated at between 100 and 125°C and high effective pressures of between 60 and 90 MPa for between 17 and 21 h. During this time between 15 and 19% pore fluid was expelled. This value is high relative to other experiments as some of the pore fluid is evolved from the dehydrating gypsum and some from the expulsion of pore fluid from pores being compacted.

EBSD analysis

Sample preparation

Petrographic thin sections were made from the experimental cores that had been cut in half along the core axis. The specimen coordinate axis X is defined as parallel to the core symmetry axis (vertical with respect to the rig), and Y is parallel to the thin section and therefore core short axis (horizontal with respect to the rig). As bassanite is metastable under normal atmospheric conditions and owing to the risk of hydration it was necessary to exclude water during the preparation of the thin sections. Thin sections were prepared at the University of Birmingham using the same procedure as documented by Hildyard *et al.* (2009*b*) and outlined here; core sections were ground to an initial starting thickness (~0·5 mm) using a blend of industrial methylated spirit and ethylene glycol; in the final stages of fine polishing, oil-based diamond suspensions blended with the methylated spirit–ethylene glycol as a coolant–lubricant were used; stages of 1 and then ¼ µm diamond paste were used on a Buehler Texmet 1000 polishing mat on a Metaserv polishing machine.

Chemo-mechanical polishing (using an aqueous suspension of 0·05 µm colloidal silica, i.e. SYTON) is normally required, to remove surface damage caused by the earlier stages of mechanical polishing, before EBSD analysis can be conducted (Lloyd, 1987; Prior *et al.*, 1996). However, because bassanite is highly soluble at all temperatures and because some of the samples contained a proportion of gypsum this procedure was omitted and EBSD analysis was conducted on samples not polished using SYTON. Samples were coated with a thin film of carbon to prevent charging (Fynn & Powell, 1979). As in previous studies on gypsum (Hildyard *et al.*, 2009*b*), good and index-able EBSD patterns were recovered from bassanite (and gypsum) even though the SYTON polishing stage had been omitted and later EBSD runs yielded acceptable rates and percentages of indexed points.

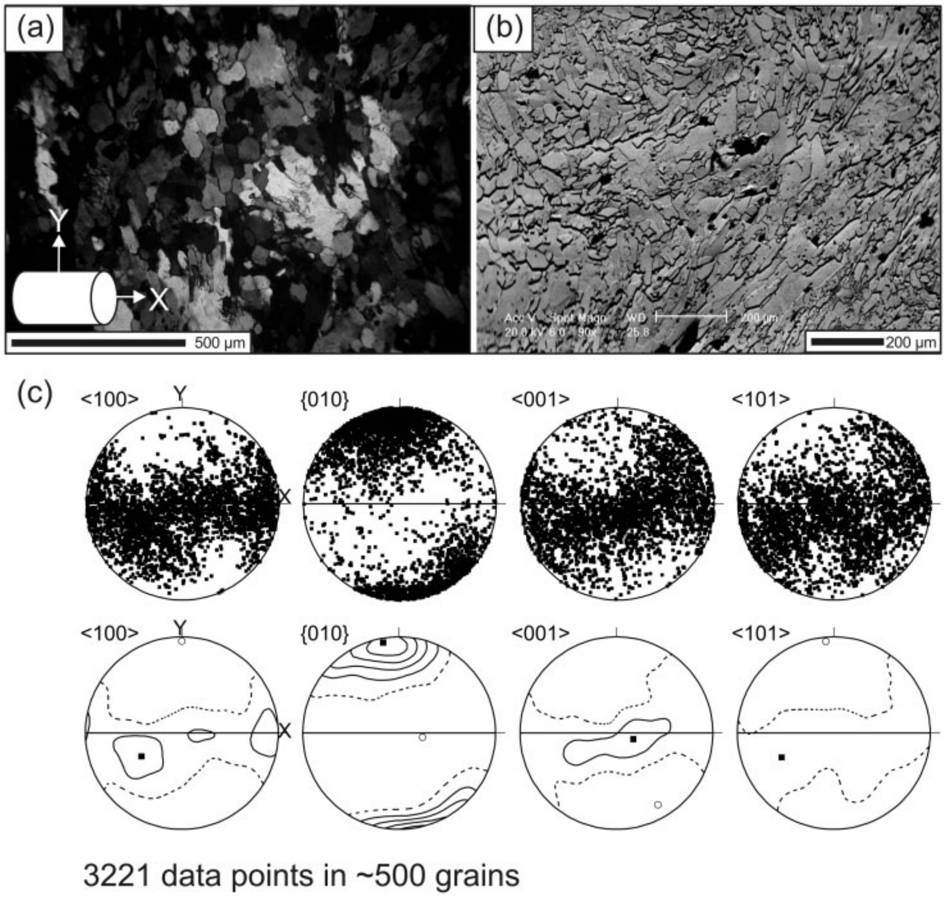

Fig. 2. Starting material, Volterra gypsum. (a) Cross-polarized light (XPL) micrograph showing representative microstructure of Volterra gypsum. (b) Backscatter electron SEM image of Volterra gypsum showing polygonal grains of gypsum with a slight shape preferred orientation. (c) Scattered and contoured (lowest value contour line is dashed; contour lines represent an increment of 1 MUD, and the maximum is indicated by a square) stereographic, lower hemisphere pole figures of the bulk CPO of an area of Volterra gypsum.

EBSD data acquisition

Full crystallographic orientation data were collected using a Philips XL30 scanning electron microscope (SEM) with a tungsten filament and a Nordlys II 20 Mhz 12 bit digital camera. The EBSD patterns were collected using the calibration parameters in Table 3 and a sample tilt of 70° counter-clockwise from horizontal. Fast data collection was important as the patterns degrade after <1 s of exposure owing to electron beam damage; in this study data were collected at a rate of 0·102 s per point. The EBSD patterns were indexed using the program Channel5 from Oxford Instrument HKL software. Samples were ‘mapped’ using automated beam scanning, where the specimen is stationary and the beam scans a user-defined area. The stage then drives to the next area and the beam scanning is resumed. The ‘maps’ are then stitched together.

Reflector files generated from eight bassanite crystal structure parameters (see Table 1) were tested in initial investigations into whether bassanite could be successfully indexed, and subsequently processed, by EBSD. As some of the samples analyzed had good basal and prismatic sections of large bassanite crystals, different crystal reference files could be tested on the same crystal. Only two crystal files yielded acceptable pattern indexing, evidenced by mean angular deviation (MAD) values below the 1–3° tolerance; one used monoclinic symmetry (Ballirano *et al.*, 2001; Table 4) and one used trigonal symmetry (Christensen *et al.*, 2008). When EBSD patterns were indexed using both of these structures, even though the fit was extremely good, both crystal files missed between one and two diffraction bands. Also, both crystal files produced the same systematic mis-indexing. No other difference between the accuracy of the crystals files could be determined and so the monoclinic crystal file of Ballirano *et al.* (2001) (Table 4) was chosen to index bassanite.

Data processing

All EBSD raw data were post processed using the HKL Technology software package Channel5. Data processing and noise reduction were performed on the original

Table 2: Parameters of the dehydration and deformation experiments of Volterra gypsum

Sample no.		Dehydration conditions				Compaction	Duration	Vol. % of expelled pore fluid	Crystal morph.	Approx. Av. Grain size ($L \times W$ μm)
		T (°C)	P_c (MPa)	P_p (MPa)	P_{eff} (MPa)	P_c max. (MPa)				
Dehydrated under low P_{eff}										
GYP37		110	14	10	4	—	5 days	8%	Euhedral	300 × 50
GYP38		120	14	10	4	—	1 day	Min. 5%	Euhedral	150 × 30
GYP43		125	100	90	10	—	18 h	5·5%	Acicular	20 × 5
Dehydrated under low P_{eff} *with subsequent compaction*										
GYP30	1st stage	140	75	73	2	—	5 h	3%	Acicular	20 × 5
	2nd stage	30	15	10	5	200	≤1 min per P_c increment	6%		
GYP 3334	1st stage	110	55	50	5	—	20 h	8%	Euhedral	125 × 25
	2nd stage	115	14	11	3			5·5%		
	3rd stage	50				50	1–10 min per P_c increment			
Dehydrated at high effective pressure (simultaneous compaction)										
GYP56		110	100	10	90	Yes	21 h	15·3%	Acicular	20 × 5
GYP57	1st stage	53–25	100	40	60	Yes	12 h	0%	Acicular	20 × 5
	2nd stage	125	110	10	100	Yes	4 h	17%		

Table 3: Summary of the EBSD calibration parameters used in the Philips SEM

Operating conditions	Philips SEM
Step size (μm)	1·5–4
Accelerating voltage (kV)	20
Beam current (nA)	3
Spot size	6
Working distance (mm)	24
Hough resolution	80
No. of reflectors	75
No. of bands detected	8
Time per frame (ms)	15
Background frames	64
Noise reduction frames	5
Binning	4 × 4
Gain	High
Scan type	Beam scan

EBSD dataset to remove non-indexed (where the software is unable to find a solution for the diffraction pattern) or mis-indexed (where the software applies the wrong solution; for example, one point of gypsum in a large grain of bassanite) data points. Correction of the systematic mis-indexing in bassanite was not conducted as ⟨101⟩ provides a robust orientation. The general noise reduction process used here within datasets with a good initial level of indexing (samples GYP3334, 37, 38 and 56) was first to replace wild spikes (i.e. an isolated mis-indexed pixel) with a zero solution (i.e. a non-indexed point); then, to refine the dataset further and to avoid introducing artefacts by growing grains past their grain boundaries, a subset of data was created that contained only the internal grain area by using band contrast or pattern quality maps to locate grain boundaries (grain boundaries have poor band or pattern quality) and exclude them from the subset. Then non-indexed points within this subset with a minimum of five indexed neighbouring pixels were replaced with a copy of the average neighbouring pixel orientation. This process was iterated until all non-indexed points with five or more indexed neighbours had been replaced, or until the edge of the subset (i.e. edge of the grain as defined by the band contrast or pattern quality threshold) was reached. Finally, to fill any remaining areas with no data the full dataset was noise reduced again, replacing non-indexed points with five or more neighbours with a common orientation. Datasets that had a very poor level of indexing were treated more carefully; wild spikes were not removed until processing up to six nearest neighbours was conducted, after which erroneous wild spikes could be removed.

Table 4: Crystal files used in this study by Channel5 to index bassanite [transformed from Ballirano et al., *(2001)] by EBSD*

Space group no.:	Space group	Point group	Schoenflies
5	C2	2	C3^2
	a	*b*	*c*
Unit cell:	17·4346 Å	6·9294 Å	12·035 Å
	α	β	γ
	90°	133·39°	90°
Atoms:	*x*	*y*	*z*
Ca	0	0·5	0
Ca	0	0·011	0·5
Ca	−0·1677	0·199	0·0703
Ca	−0·6648	0·165	−0·4431
S	−0·2493	0·499	−0·2509
S	−0·9183	0·164	−0·6936
S	−0·4146	0·185	−0·1864
O	−0·984	0·211	−0·857
O	−0·473	0·23	−0·348
O	−0·315	0·616	−0·241
O	−0·816	0·62	−0·741
O	−0·332	0·044	−0·136
O	−0·858	−0·015	−0·653
O	−0·178	0·366	−0·121
O	−0·673	0·376	−0·615
O	−0·361	0·359	−0·089
O	−0·838	0·317	−0·6
O	−0·991	0·161	−0·672
O	−0·491	0·103	−0·183
H	0	0·843	0
H	−0·353	0·004	0·6

The bassanite crystal setting in the table is transformed (using software from Aroyo *et al.*, 2006*a*, 2006*b*) from the original setting of Ballirano *et al.* (2001) to a standard setting crystal so that it can be used in Channel5.

RESULTS

Starting material

A polished section of a core of Volterra gypsum was used to measure the bulk CPO of the original, pre-tested starting material. Reflected light microscopy showed the grains to be fairly equant and subhedral, with little evidence of twinning (Fig. 2a shows a representative microstructure in transmitted light). There are areas where grains show some alignment outlining an overall weak shape preferred orientation. A backscatter electron image of the area mapped using EBSD further highlights the slight shape preferred orientation (Fig. 2b). The bulk crystallographic preferred orientation was measured across an area of representative microstructure at a step size of 10 μm. The data were then plotted on lower hemisphere, stereographic projections as one point per measured grain (Fig. 2c). A strong preferred orientation can be seen with data clustered around *Y* (corresponding to the short axis of the core) in the {010} pole figure and corresponding girdles in ⟨100⟩ and ⟨001⟩.

Optical microscopy

Three types of bassanite were distinguished, which we refer to as euhedral, acicular and cloudy.

Three of the samples (GYP3334, 37 and 38) contain euhedral crystals of bassanite which exhibit good basal and prismatic sections (see Fig. 3a, I) and predominantly straight grain boundaries. Euhedral bassanite grains up to 2 mm occur rarely (e.g. Fig. 3a, I) but on average the grain size is ∼200–600 μm. The bassanite grains display high first- to low second-order interference colours (brown–orange through to purple–blue) in cross-polarized light and are colourless in plane-polarized light.

'Cloudy' bassanite is defined as areas that are predominantly bassanite but that contain very fine-grained, grey in cross-polarized light, relict gypsum. This is easily distinguishable from pure bassanite as the cloudy bassanite has low first-order grey interference colours in cross-polarized light owing to the presence of relict gypsum. In these three samples (GYP3334, 37 and 38) it is present in variable quantities, and the average cloudy bassanite grain size (<100 μm) is much finer than that of euhedral bassanite. In these samples the well-formed bassanite crystals are concentrated into discrete domains (e.g. Fig. 3b) that are ∼90% pure bassanite. Surrounding these areas are regions where the proportion of euhedral bassanite to cloudy bassanite is 60/40. In these regions cloudy bassanite is acicular and tends to be elongate perpendicular to the core axis. As well as single grains, the 'patches' of euhedral bassanite and surrounding 'pathways' of cloudy bassanite are aligned perpendicular to the core axis (this is seen particularly well in Fig. 3b).

Samples GYP30, 43, 56, and 57 (Fig. 3a, II) are composed of bassanite crystals that have a very acicular appearance. Single grain boundaries are hard to define for such needles but the overall grain size is very fine (<∼50 μm). As in the samples discussed above, there are discrete zones that are composed primarily of pure bassanite (∼60%) and areas separating these that are composed of 'cloudy' bassanite (up to 90%). In samples GYP30, 43, and 57 the gypsum is very fine grained and acicular in appearance. The discrete zones do not occur around the edge of the sample in GYP30 and 43; instead, there is a region of 50/50 pure/cloudy bassanite, with bassanite needles being preferentially aligned perpendicular to the core axis. In GYP56 (Fig. 3d) the boundary between an

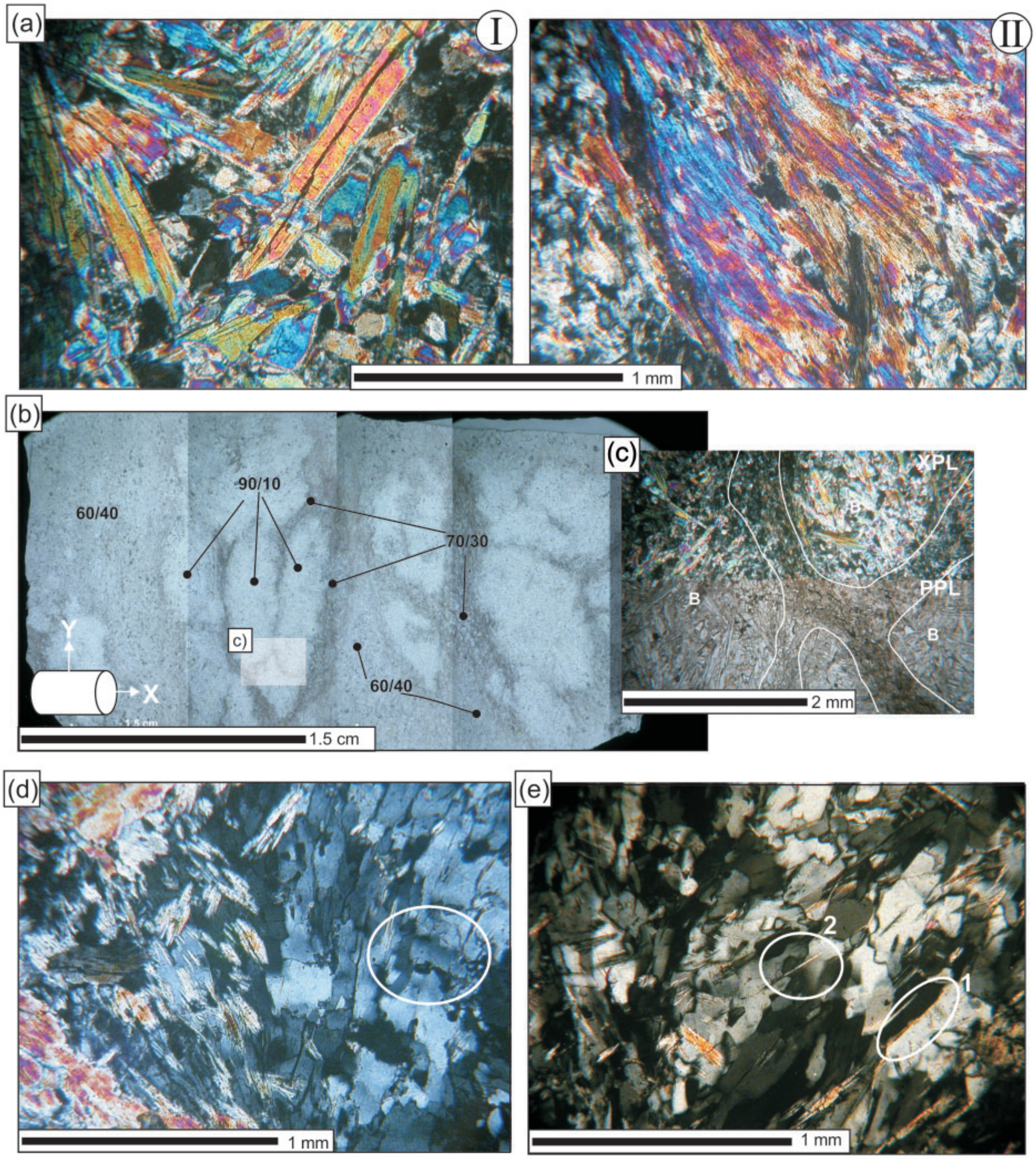

Fig. 3. Optical micrographs of representative features within the samples after the experiments. (a) XPL micrograph showing examples of the two morphological crystal types: (I) large, euhedral bassanite grains (sample GPY37); (II) small, acicular bassanite grains (sample GYP30). (b) Plane-polarized light (PPL) micrograph of a full thin section (GYP3334) with relative percentages of pure bassanite/cloudy bassanite in various zones in the thin section. (c) XPL and PPL micrograph of a detailed area [shown in (b)] of microstructure. (d) XPL image of the boundary between bassanite and gypsum (sample GYP56), showing undulose extinction in gypsum (outlined). (e) XPL image of acicular bassanite needles growing along (ellipse 1) and cross-cutting (ellipse 2) grain boundaries (sample GYP56).

acicular bassanite region and euhedral gypsum is seen. Here, the gypsum is of a coarse grain size (~100–500 μm), has euhedral grains and irregular grain boundaries, and displays undulose extinction. In some places bassanite needles can be seen to have grown along gypsum grain boundaries (grain circled in Fig. 3e) whereas in other areas bassanite needles cross-cut gypsum grain boundaries and grains.

EBSD analysis

Bassanite mis-indexing

Initial EBSD maps of bassanite (Fig. 4) revealed a pseudo-trigonal systematic mis-indexing problem. Single pixels within a bassanite crystal were found to be systematically mis-indexed by rotations around ⟨101⟩ of 60°, 120° and 180° (Fig. 4a and b). The level of mis-indexing is significant. However, by comparing a number of transverse (approximately basal) and prismatic sections of bassanite crystals it was found that the ⟨101⟩ direction provided reliable orientations. This was determined in the following way. In Fig. 4c a prismatic section of a crystal (labeled PC1) is seen with its long axis oriented at ~45° to the long axis of the EBSD map; assuming the long axis of the prismatic section of the crystal corresponds to a rational crystallographic direction then on a pole figure a point would plot close to the primitive circle and fall along the trace orientation of the crystal's long axis. In this case the ⟨101⟩ direction corresponds to the long axis of the crystal and plots where one would expect in the pole figures (Fig. 4d). This logic is true for transverse sections, where the crystal long axis, in this case ⟨101⟩, intersects the plane of section at ~90° and therefore would plot close to the centre of a pole figure (prismatic pole figures in Fig. 4d). Therefore, data plotted in ⟨101⟩ pole figures can be considered robust and reliable, and as such allow comparative analysis of orientation data between samples to be made.

Grain analysis

EBSD maps (2–3 μm step size) were taken of samples GYP37 and GYP38 to map in detail the microstructure of well-formed bassanite crystals. EBSD maps with ~75% bassanite indexing were obtained (Fig. 4c). Crystallographic data for single bassanite prismatic and transverse sections were plotted onto lower hemisphere stereographic pole figures (Fig. 4d). In the pole figures of the prismatic sections there is no spread of data in the ⟨100⟩, {010} and ⟨001⟩ pole figures (ignoring the systematic repetition of orientations in each). In pole figures of the transverse sections there is a clear and consistent dispersion of data in the ⟨100⟩, {010} and ⟨001⟩ pole figures around the ⟨101⟩ axis. In these pole figures one of the systematic mis-indexed orientations (Fig. 5a) was chosen in each transverse section plot (there were no consistent criteria for which cluster was chosen in each case) and used to examine changes in misorientation across the crystal (Fig. 5c). The resulting texture component maps clearly show gradual changes in misorientation across the transverse sections.

Crystallographic preferred orientation (CPO)

EBSD maps were collected and the full dataset was plotted on lower hemisphere, stereographic scattered and contoured pole figures for all the samples tested (Fig. 6). Half-widths and cluster sizes vary for each sample and contour lines represent increments of multiples of uniform distribution, up to the stated maximum. Viewing only the ⟨101⟩ pole figures (as this is the most reliable direction not affected by mis-indexing) there is a distinct preferred orientation. Samples GYP3334, GYP37, GYP38, GYP56 and GYP57 show clustering of ⟨101⟩ axis parallel or subparallel to Y, whereas GYP30 and GYP43 show a clustering of ⟨101⟩ axis perpendicular to Y and parallel to X.

Juxtaposed gypsum and bassanite textures

An EBSD map of a boundary between gypsum-rich and bassanite-rich domains in sample GYP56 (Fig. 3d) was taken. The orientation contrast image in Fig. 7a shows low-relief gypsum next to a higher relief area of bassanite. Band contrast and Euler angle maps (Fig. 7b) further highlight the difference in form between the gypsum (left), which is mostly equant, and the bassanite, which is composed of elongated crystals (right). Pole figures of gypsum show a strong preferred orientation, where gypsum *c*-axes are strongly clustered in two maxima oblique to Y and contained in a plane perpendicular to X (Fig. 7c). In the bassanite ⟨101⟩ pole figure (*c*-axis in trigonal symmetry) a girdle-like distribution of axes is seen perpendicular to X and with a maximum parallel to Y.

DISCUSSION

Several interesting observations can been made regarding the texture of the original starting material, the texture and morphology of bassanite formed during the course of the experiments, and a comparison between the textures seen in the remaining and deformed gypsum and bassanite (after gypsum) in the same sample.

Starting material

Many workers (e.g. Ko *et al.*, 1995; Olgaard *et al.*, 1995; Barberini *et al.*, 2005) have described Volterra gypsum as having a 'homogeneous' texture. Although this may be true on a large scale, at the scale of the cores in this study, with a length range of 30–50 mm, a degree of heterogeneity exists. In the present study, a test was conducted to see if the starting material does have an initial texture prior to any period of testing. A strong and measurable bulk CPO is observed in the specimen used (Fig. 2). Gypsum is, however, relatively susceptible to deformation at low temperatures (in the region of 40–50°C), with kinking and fracturing observed experimentally and undulose extinction and subgrains common in nature, suggesting plasticity. As such very little strain or low temperatures can potentially alter, create or destroy a crystallographic fabric. An indication of the likely heterogeneity of the initial CPO is given by the difference between that in the

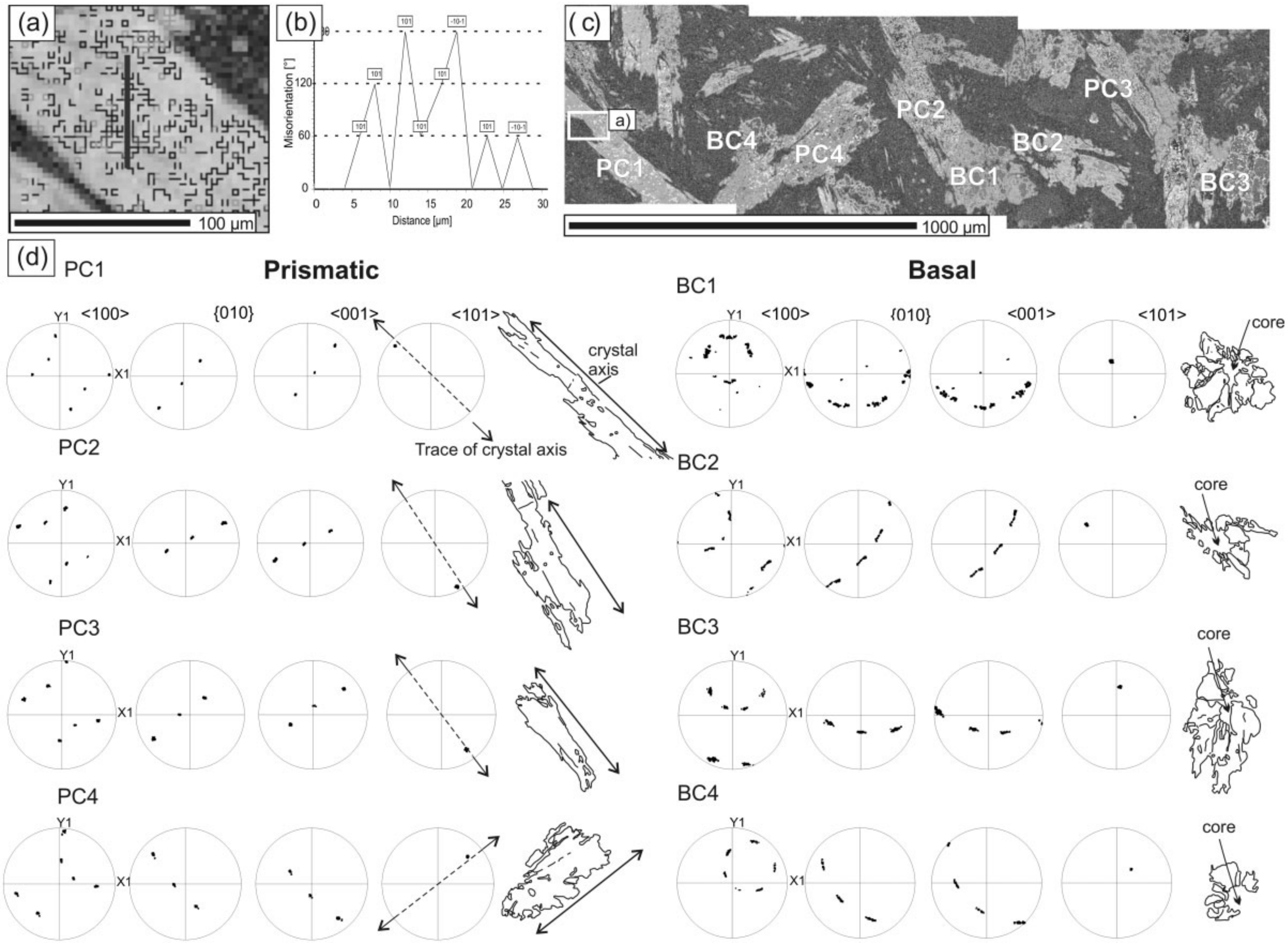

Fig. 4. Systematic mis-indexing associated with bassanite (from sample GYP37). (a) Special boundary map of a small portion [box in (c)] of a prismatic section of a crystal. Lines separate different indexed points that have a misorientation relationship of 60° rotations around ⟨101⟩. (b) A misorientation profile taken across the special boundaries in (a) (black line); here the misorientation axis ⟨101⟩ and angles 60°, 120° and 180° are clearly defined. (c) Euler orientation and band contrast maps of a sample with good prismatic and basal sections of bassanite. The location of the crystal studied in detail in (a) is indicated. Labels correspond to the pole figures in (d). (d) Stereographic, lower hemisphere pole figures of single prismatic and transverse bassanite crystals. A clear rotation axis is seen in the ⟨101⟩ pole figure, and a spread of data relating to the 60° incremental misorientation is seen in ⟨100⟩, {010} and ⟨001⟩ pole figures; schematic diagrams of each grain plotted in the pole figures show a good correlation between the near-horizontal crystal axis (⟨101⟩) in the prismatic sections and the near-vertical to high-angle ⟨101⟩ axis in the transverse sections.

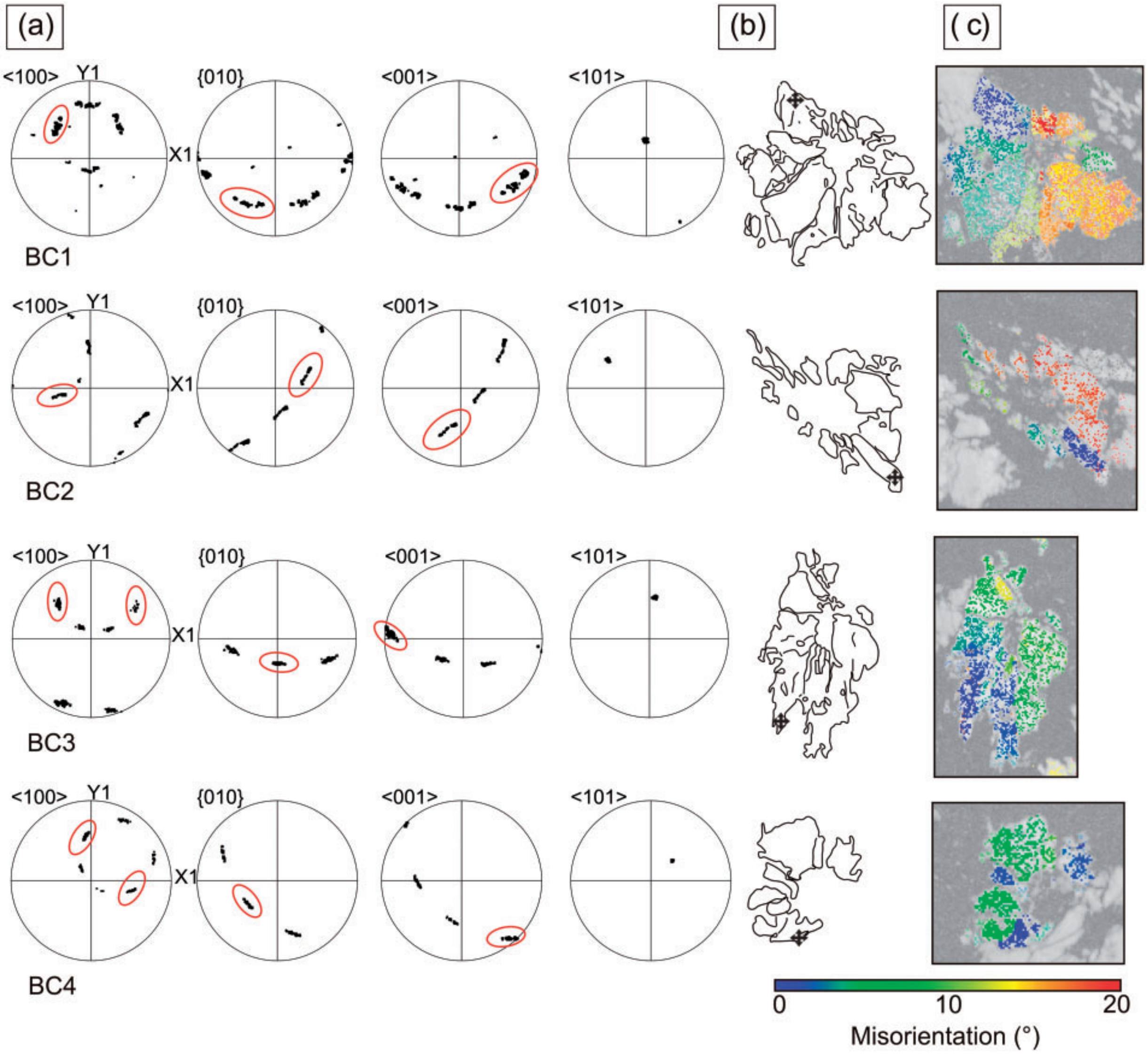

Fig. 5. (a) Stereographic, lower hemisphere pole figures of the bassanite transverse sections shown in Fig. 4d. The data points outlined in red are those used to construct the texture component maps in (c). (b) Schematic sketches of the transverse sections for which data are plotted on pole figures in (a) and shown in (c). The cross is the reference point used to construct the texture component maps in (c). (c) Texture component maps of bassanite transverse sections showing both continuous and discontinuous orientation variations across each grain (relative to the reference point).

starting material, which shows a girdle in ⟨001⟩ (Fig. 2) and that in GYP56, which shows two clusters in ⟨001⟩ (Fig. 7).

Bassanite crystal morphology

Initial observations of the samples used in this study show there are two distinct populations of bassanite based on crystal morphology and grain size. Samples GYP37, 38 and 3334 (Fig. 3a, I) exhibit fairly euhedral bassanite crystals forming an inequigranular, decussate aggregate with an overall coarser grain size of 200–600 μm. The remaining samples studied (Fig. 3a, II) have an acicular, equigranular aggregate appearance with an overall much finer grain size of <~50 μm. This observation is consistent with the findings of Singh & Middendorf (2007), who recognized two morphologies of bassanite; one which they termed ‘flaky particles’ and another that forms euhedral (or idiomorphic) crystals. Singh & Middendorf (2007) related the different morphologies to the α- or β-form of bassanite, respectively. They showed that the α-bassanite form, prepared by dehydrating gypsum under a high partial pressure of water vapour (e.g. above 45°C

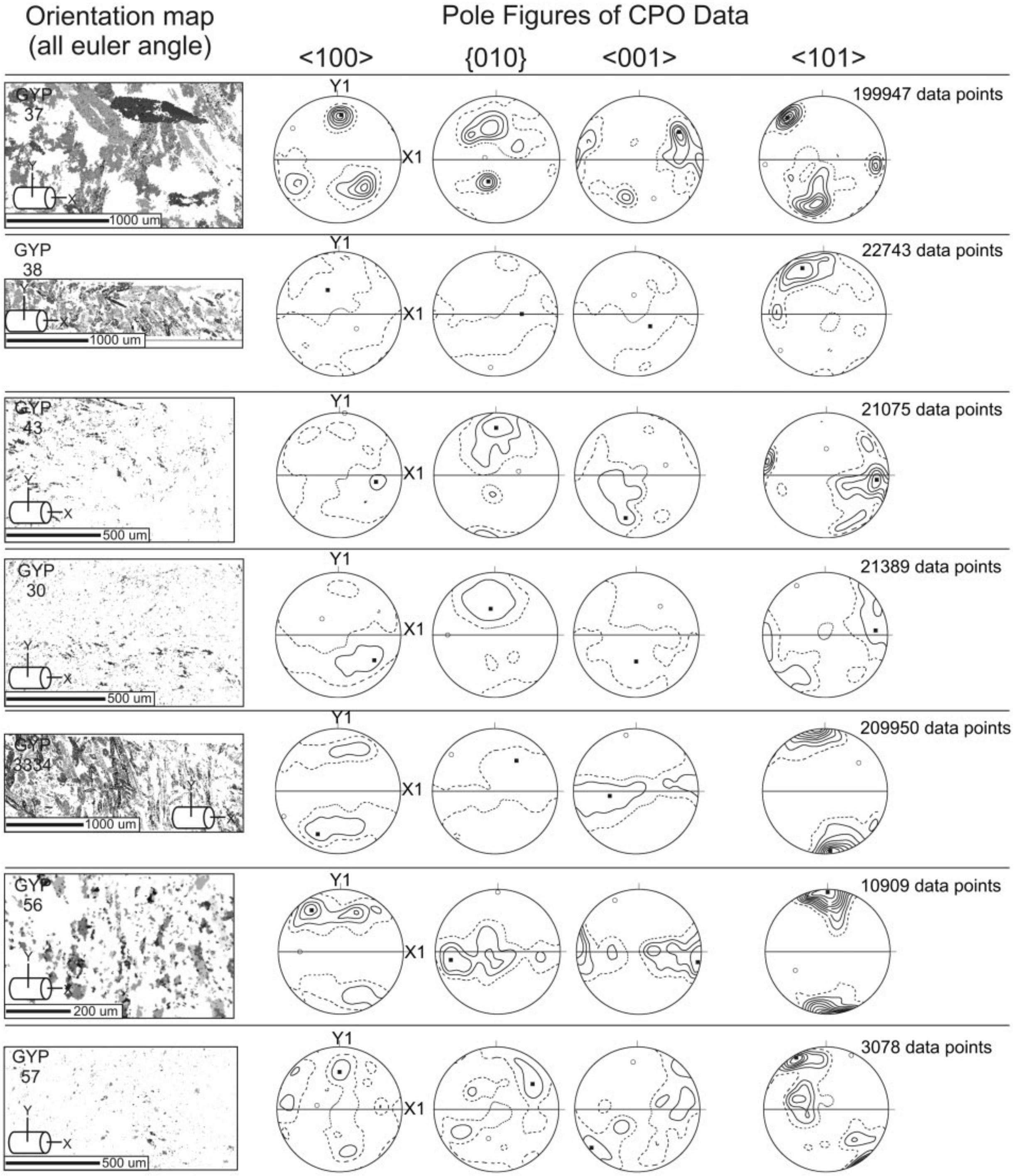

Fig. 6. Crystallographic preferred orientation of bassanite grains from all samples. First column shows orientation maps (Euler 1) and highlights the density of data; each map contains in excess of 300 grains, except for GYP37, which has ~150 grains; the second column shows contoured pole figures (lower hemisphere, stereographic) of selected crystallographic elements, using every indexed pixel; the third column shows the robust and usable ⟨101⟩ contoured pole figures (each contour line represents an increment of one multiple of uniform distribution, up to a maximum indicated by the square). The pole figures in bassanite should be viewed with a degree of caution owing to mis-indexing problems (see text for details).

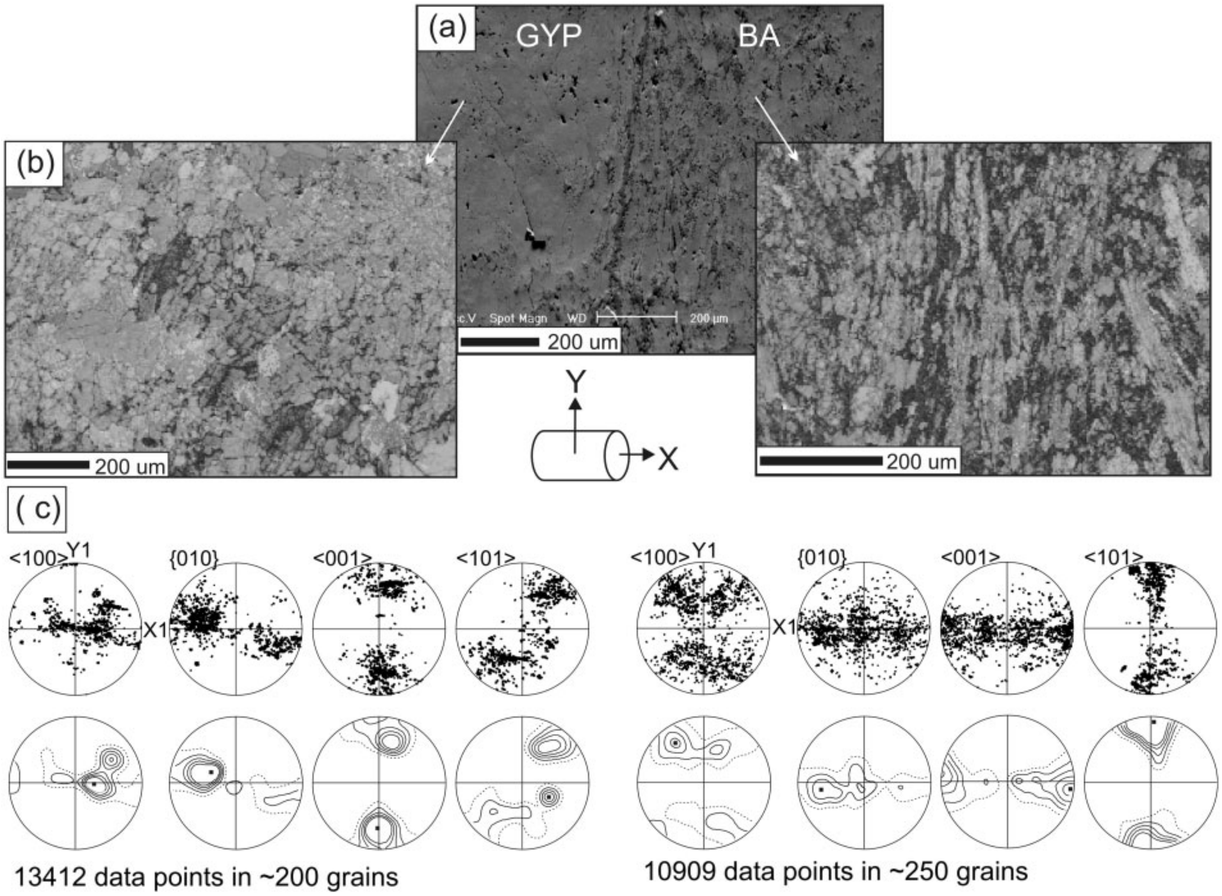

Fig. 7. Comparison between gypsum and bassanite fabrics within the same sample, GYP56. (a) Orientation contrast image of the area mapped using EBSD; a boundary between gypsum (GYP) and bassanite (BA) can be seen down the centre of the image. (b) Orientation maps (all Euler and pattern quality) of the areas mapped in gypsum and bassanite. (c) Stereographic, lower hemisphere pole figures showing scattered and contoured data (half-width 20°, cluster size 5°) from gypsum (left) and bassanite (right) in each area, using every indexed pixel in each figure.

in acid or salt solutions, or above 97·2°C in water at elevated pressures), forms euhedral crystals with sharp crystal edges. In contrast, the β-bassanite form, prepared by dehydrating gypsum under a low water vapour partial pressure (i.e. in dry air or vacuum, between 45 and 200°C), forms flaky particles made up of small crystals. This difference in morphology was also noted in investigations by Freyer & Voigt (2003), where they observed fine-grained β-bassanite (trigonal) fibres that have higher thermal stability (dehydrating between 100 and 160°C), disc-like crystals (with short *c*-axis) with lower thermal stability (dehydrating between 90 and 125°C) and hexagonal columns of α-bassanite. All the samples in the present study were dehydrated in the presence of pore fluid pressure under 'wet' conditions and between 100 and 150°C. These conditions correspond fairly closely to those within which Singh & Middendorf (2007) recognized euhedral crystals of α-bassanite.

Bassanite is stable only at pressures above ~230 MPa and temperatures above 80°C (McConnell *et al.*, 1987). The bassanite seen in this study has been produced at P–T conditions that lie within the anhydrite stability field and is therefore metastable. The reaction that produced bassanite can be overstepped up T or down P from the (metastable) gypsum–bassanite equilibrium line by varying amounts (McConnell *et al.*, 1987) (Fig. 8). On the equilibrium line, no bassanite should be produced; to its right there is a free energy decrease ΔG, which will be a primary influence on nucleation and growth rates (Yardley, 1989; Lasaga, 1998). Thermodynamics predicts that nucleation rates will be faster and hence ultimate grain size finer, for larger oversteps in ΔG and/or higher temperatures. Bearing in mind that the grain-size estimates (Table 2) are approximate, samples GYP37, 3334, and 38 do indeed show decreasing grain size with increasing temperature in the 110–120°C range, and the higher temperature

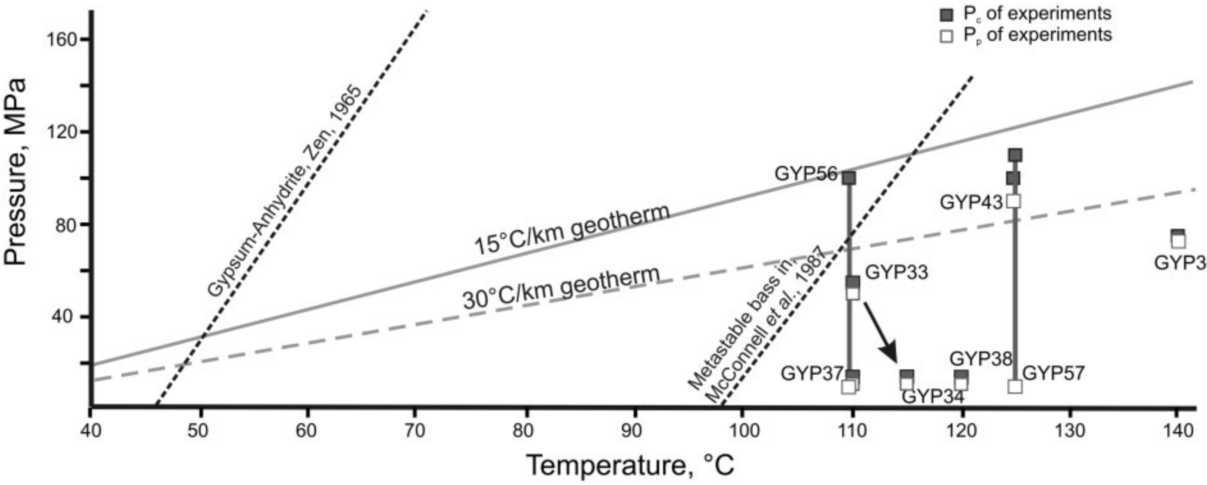

Fig. 8. Pressure–temperature graph showing the gypsum-out curve from Zen (1965), the metastable bassanite-in curve of McConnell *et al.* (1987), $30^{\circ}\mathrm{C\,km^{-1}}$ and $15^{\circ}\mathrm{C\,km^{-1}}$ geotherms and the confining (P_c) and pore fluid (P_p) pressure that each sample was subjected to relative to the geotherms. Geotherms show lithostatic pressure for the stated temperature gradients. Fluid pressure may be less than lithostatic pressure in nature, as our experiments reflect. The arrow shows that the conditions of GYP34 were imposed on the product of experiment GYP33.

runs (43, 57 and 30) continue that trend up to 125–140°C. GYP56 is anomalous in having a small grain size for a small overstep, but this is because grain size provides an inverse relationship to number of nuclei only when the reaction is complete. This run was only partially dehydrated and for a short time relative to other samples and shows relatively little transformation.

Temperature affects nucleation and growth rates directly (e.g. via an activation energy term) and indirectly via its effect on ΔG. Pressure will also control ΔG—although its effect is not immediately obvious from the data in Table 2; for example, GYP43 and 57 show much the same grain size. However, GYP33 showed virtually no reaction at 110°C and 55 MPa fluid pressure (this is why conditions were changed later in that experiment) whereas GYP37, at 110°C and just 10 MPa fluid pressure, showed a significant (although slow) reaction rate. The lower pore fluid pressure leads to a larger ΔG for the same temperature, and thus a faster reaction (Llana-Funez *et al.*, in preparation).

Quality of bassanite EBSD data

The present study has shown that measurement of crystallographic preferred orientation by EBSD is possible for bassanite crystals and our work shows that a strong CPO is demonstrably measurable within these experimentally generated samples. This is the first time that the full crystallographic preferred orientation of bassanite has been measured using EBSD. However, the quality of the EBSD maps, in terms of total indexing, for the samples is variable (see Fig. 6). Samples containing large euhedral bassanite crystals had the best indexing rates (38–45%) whereas the samples containing small acicular bassanite crystals had much worse indexing rates (2–7%). The reason for this is likely to be a combination of variability in polishing quality and crystal morphology. The acicular samples are essentially composed of many small single crystals; a high density of grain boundaries per unit area affects the quality of the indexing rates because polishing does not remove damage at grain boundaries easily.

Bassanite microstructure and growth

The formation of large euhedral bassanite crystals presents an opportunity to investigate growth mechanisms. Variable growth rates of different crystallographic faces owing to directional differences in bonding properties are the basis for the establishment of crystal habit (Lasaga, 1998). In prismatic sections the long axes of the bassanite crystals are parallel to ⟨101⟩ (Fig. 4c). As the samples were indexed using a monoclinic crystal setting but display pseudotrigonal symmetry represented by the systematically mis-indexed clusters repeated at 60° intervals, we can also say that the ⟨101⟩ axis in a trigonal setting is equivalent to the crystallographic *c*-axis. This implies that bassanite has grown preferentially in the direction of ⟨101⟩, producing elongate prisms in agreement with Follner *et al.* (2002). Those workers found that bassanite predominantly crystallizes in the form of hexagonal prisms parallel to the *c*-axis (in a trigonal setting) terminated by rhombohedral faces.

Small circle dispersions of data from basal sections can be seen in the ⟨100⟩, {010} and ⟨001⟩ pole figures, corresponding to a clear and consistent ⟨101⟩ misorientation axis (Fig. 4d). Though incomplete because of non-indexed points, the maps in Fig. 6c show some smooth variations in orientation but also some sharper boundaries that are likely to be subgrain walls. These boundaries are best seen in sections transverse to the laths and we infer that the boundaries are parallel to the laths. Thus the bassanite grains are actually bundles of long thin subgrains misoriented by small angles around ⟨101⟩. Similar microstructures have been recorded in other studies. Quartz 'lineage structures' (Carstens, 1968) are essentially low-angle tilt boundaries parallel to the quartz *c*-axis. In omphacite, elongate subgrains forming fan-like structures occur where ⟨001⟩ is parallel to the long axis of the subgrains and around which misorientations occur (McNamara, 2009). Timms *et al.* (2009) recorded somewhat similar microstructures in natrojarosite, although in their work the *c*-axis is preferentially perpendicular to the crystal long axes.

Carstens (1968) and Timms *et al.* (2009) attributed the microstructures to growth rather than deformation, and this is also our preferred explanation. In quartz, growth can introduce dislocations. Once established in a lattice, a dislocation that intersects a growing surface cannot be 'healed'; that is, it will persist as the surface advances. If there are enough dislocations to produce lattice distortion measurable with EBSD, that distortion will persist as the crystal grows. Carstens (1968) further suggested that dislocations can actually rearrange into low-angle boundaries during growth (a process akin to recovery). Again, these low-angle boundaries will persist during further growth. Hence, we attribute the bassanite low-angle substructures to a combination of (1) persistence of lattice defects formed early in grain growth and (2) possibly, later movement of growth dislocations into low-angle boundaries. It is possible but unproven that the bassanite defects were inherited from gypsum (see below).

Spatial distribution of bassanite

In all samples (with the exception of GYP56, which is only partially dehydrated and has little bassanite) bassanite crystals are, to a variable extent, clustered. This can be seen particularly well in GYP3334 (Fig. 3b) where, in the plane-polarized light micrograph, a network of darker areas surrounds higher relief areas. The darker areas are composed of smaller amounts of fine-grained pure bassanite interspersed with cloudy bassanite and relict gypsum (60/40 pure bassanite/cloudy bassanite) in contrast to the lighter areas of virtually pure large, euhedral bassanite grains. This heterogeneity could be explained by the establishment of large-scale fluid pathways that develop as one area of the sample begins to dehydrate ahead of another, thus setting up internal pressure gradients and driving the process.

Bassanite CPO: inheritance from gypsum

A direct comparison between the crystallographic textures present within gypsum prior to dehydrating to bassanite and the resultant bassanite textures was possible in one of the samples tested. In sample GYP56 a distinct boundary (or an arrested reaction front) was found between an undehydrated area of gypsum and an area of bassanite. The gypsum in this sample displayed undulose extinction (Fig. 3d), pointing towards a degree of intracrystalline plasticity, which has also been observed in previous studies (i.e. Barberini *et al.*, 2005). This interpretation is further confirmed by the presence of a strong CPO measured in the gypsum-rich areas of this sample.

Comparison of this gypsum CPO and the adjacent bassanite CPO shows that bassanite ⟨101⟩, that is, the pseudo-trigonal symmetry axis, correlates with gypsum ⟨001⟩ (Fig. 7c). This would suggest that the CPO from the gypsum had a controlling effect on the CPO of the newly formed bassanite. For example, if the orientations of bassanite nuclei (within gypsum grains or at grain boundaries) were controlled by gypsum lattice orientations, bassanite would inherit aspects of the gypsum CPO. We are reluctant to correlate other bassanite crystallographic directions with those in gypsum because of bassanite indexing problems. At a general level, however, our observation agrees with that of Freyer & Voigt (2003), who suggested that as the dehydration reaction from gypsum to β-bassanite is topotactic, the crystallographic [010] and [001] axes in gypsum become the new [001] axis in β-bassanite (trigonal). This idea could in principle be tested, except that bassanites have, since nucleation, grown so as to cross-cut gypsum boundaries (as in GYP56, Fig. 3e) and the identification of a 'parent' gypsum grain becomes ambiguous. Nevertheless, the topotactic relationship is our preferred explanation for the bassanite CPO.

Bassanite CPO: variability between samples

The ⟨101⟩ pole figures show strong and consistent fabrics; this direction is therefore used as a reference crystallographic element for comparison between specimens. Samples GYP3334, 37, 38, 56 and 57 have ⟨101⟩ poles clustered parallel to Y; this indicates that bassanite crystals are preferentially oriented with the crystallographic long axis perpendicular to the long axis of the sample. Samples GYP30 and 43 have the data clustered around X, indicative of the crystal long axis being oriented parallel to the long axis of the sample. In summary, bassanite CPOs show variable orientation; this is simply explained by variable gypsum CPOs in the original cores and their subsequent influence on oriented bassanite nucleation and/or growth.

Geological implications

Our work focuses on specific issues in the behaviour of gypsum and general aspects of how dehydration reactions progress in the Earth.

The experimental conditions at which the dehydration tests were run are a direct replica of burial pressure and temperature conditions expected in nature (see geothermal gradients and the location of tests in P–T space in

Fig. 8) but reaction timescales are shorter. In nature, anhydrite replaces gypsum during burial and heating but secondary gypsum is commonly found replacing anhydrite (Warren, 2006) and may contribute to sealing of hydrocarbon reservoirs (Alsharhan, 2003; Jiang *et al.*, 2010). Our study is directly relevant to understanding the effects of fluid pressure fluctuations on gypsum seal integrity and on gypsum décollements. Rapid fluid pressure reductions may be triggered by earthquakes, and we then expect bassanite to form, exactly as in our experiments.

Our experiments show that substantial porosities will build up even when lithostatic pressure is greater than the fluid pressure and compaction is expected. The dehydration product will thus be very permeable, with implications for seal quality above a hydrocarbon reservoir or potential CO_2 repository. The experiments also show that dehydration progress and consequent porosity development may be heterogeneous (e.g. Fig. 3b and c). A better understanding of such heterogeneities is required to allow upscaling of average permeability.

Through time, this porosity will decrease. On short timescales, the presence of porosity will weaken the rock: critical-state soil mechanics in porous materials relates a decrease of the stress at the yield point with an increase in porosity (Wood, 1990; Cuss *et al.*, 2003). To some extent, this mechanical effect is independent of the shape or arrangement of the particles, which are assumed to be sub-spherical. However, in dehydrated serpentinites, the spatial arrangement of olivine grains in a honeycomb pattern when dehydration occurs at high effective pressure has an effect on total strength (Rutter *et al.*, 2009). In our EBSD analysis we have shown that bassanite sometimes grows with a CPO and a strong alignment of acicular crystals. Such alignment is likely to affect the compaction behaviour.

On longer timescales, compaction may also occur by diffusion creep processes, with a consequent strong dependence on grain size (de Meer & Spiers, 1995, 1997). Our experiments show that at high temperatures and/or large pressure 'understeps', grain size is smaller. These porous but fine-grained aggregates will undergo chemical compaction quickly. In contrast, coarser aggregates produced at modest oversteps may take longer to compact, and may provide highly permeable pathways for longer.

Each of these points illustrates general aspects of behaviour during dehydration reactions in the Earth. Dehydration of hydrated phases in nature has often been portrayed as the precursor or inducer of seismicity deep in the crust and mantle (Raleigh & Paterson, 1965; Meade & Jeanloz, 1991; Miller *et al.*, 2003). For brittle behaviour to operate at great depth, there is an interplay between porosity development from reaction, high pore fluid pressure to maintain the porosity, and some trigger that allows the fluid to escape and porosity to collapse, resulting in brittle instability. The porosity, grain size and CPO of the reaction products will influence permeability and strength in other reactions as well as in gypsum to bassanite.

There are two final aspects of our experiments that have general significance. First, the CPO in bassanite is inferred to be mimetic on that of gypsum—in other words the CPO is inherited. Commonly, CPO in a mineral is interpreted as being due to plastic deformation within the stability field of that mineral. The possibility of inheritance, when there is some structural similarity between reactants and products, might influence the interpretation of deformation and metamorphic events in tectonites. The bassanite shows internal substructures developed during growth (Fig. 5). These are not stable and indicate a driving force sufficient to grow bassanite even when that has some excess free energy because of the substructures. It is likely that the substructures are a function of the amount of overstep and could, after further investigation, be used to infer reaction overstep and kinetics. This may be the case for substructures in other minerals (e.g. omphacite in eclogites; McNamara, 2009), with the potential for new insights into reaction rate and mechanism.

CONCLUSIONS

The interpretation of microstructural observations and crystallographic orientation (and misorientation) data from EBSD analysis of bassanite produced during experimental deformation and dehydration of gypsum allows the following conclusions to be drawn.

(1) Two distinctly different morphologies of bassanite are formed; large, euhedral grains and small acicular grains. The different morphologies may be linked to the degree of overstepping experienced in the dehydration reaction.
(2) Pseudotrigonal bassanite reaction products were successfully indexed using EBSD and a monoclinic crystal setting and are shown to have a strong CPO.
(3) Bassanite grows fastest in the ⟨101⟩ direction (equivalent to the trigonal *c*-axis) in single crystals and has a growth microstructure influenced by 'grown-in' dislocations and subgrain walls parallel to that axis.
(4) Bassanite grows topotactically from parental gypsum, causing inheritance of pre-existing CPOs.

ACKNOWLEDGEMENTS

We gratefully thank D. Mainprice, S. Reddy and N. Timms for constructive reviews, which have improved this paper.

FUNDING

R.C.H. was funded by a Natural Environment Research Council (NERC) studentship, research grant number

NER/S/A/2005/13332; the gypsum experiments were funded through NERC grant NE/C002938/1 (S.L.-F., J.W., D.R.F.); S.L.-F. acknowledges additional funding from research grant RYC-2008-02067 during writing and publication of this paper.

REFERENCES

Abriel, W. (1983). Calcium-sulfate subhydrate, $CaSO_4.0.8H_2O$. *Acta Crystallographica Section C-Crystal Structure Communications* **39(AUG)**, 956–958.

Abriel, W. & Nesper, R. (1993). Determination of the crystal-structure of $CaSO_4(H_2O)0.5$ by X-ray-diffraction methods and potential-profile calculations. *Zeitschrift Fur Kristallographie* **205**, 99–113.

Alsharhan, A. S. (2003). Petroleum geology and potential hydrocarbon plays in the Gulf of Suez rift basin, Egypt. *AAPG Bulletin* **87(1)**, 143–180.

Aroyo, M. I., Kirov, A., Capillas, C., Perez-Mato, J. M. & Wondratschek, H. (2006*a*). Bilbao Crystallographic Server ii: Representations of crystallographic point groups and space groups. *Acta Crystallography* **A62**, 115–128.

Aroyo, M. I., Perez-Mato, J. M., Capillas, C., Kroumova, E., Ivantchev, S., Madariaga, G., Kirov, A. & Wondratschek, H. (2006*b*). Bilbao Crystallographic Server i: Databases and crystallographic computing programs. *Zeitschrift für Kristallographie* **221(1)**, 15–27.

Ballirano, P., Maras, A., Meloni, S. & Caminiti, R. (2001). The monoclinic I2 structure of bassanite, calcium sulphate hemihydrate ($CaSO_4.0{\cdot}5H_2O$). *European Journal of Mineralogy* **13(5)**, 985–993.

Barberini, V., Burlini, L., Rutter, E. H. & Dapiaggi, M. (2005). High-strain deformation tests on natural gypsum aggregates in torsion. In: Bruhn, D. & Burlini, L. (eds) *High-Strain Zones: Structure and Physical Properties*. London: Geological Society of London, Special Publications, **245**, 277–290.

Bezou, C., Nonat, A., Mutin, J. C., Norlund Christensen, A. & Lehmann, M. S. (1995). Investigation of the crystal structure of $[\gamma]$-$CaSO_4$, $CaSO_4 + 0{\cdot}5\ H_2O$, and $CaSO_4 + 0{\cdot}6\ H_2O$ by powder diffraction methods. *Journal of Solid State Chemistry* **117(1)**, 165–176.

Boeyens, J. C. A. & Ichharam, V. V. H. (2002). Redetermination of the crystal structure of calcium sulphate dihydrate, $CaSO_4 + 2H_2O$. *Zeitschrift für Kristallographie* **217**, 9–10.

Bushuev, N. N. & Borisov, V. M. (1982). X-ray-diffraction study of $CaSO_4$+$0.67H_2O$. *Zhurnal Neorganicheskoi Khimii* **27(3)**, 604–609.

Carstens, H. (1968). The lineage structure of quartz crystals. *Contributions to Mineralogy and Petrology* **18**, 295–304.

Chen, C. C., Liu, L. G., Lin, C. C. & Yang, Y. J. (2001). High-pressure phase transformation in $CaSO_4$. *Journal of Physics and Chemistry of Solids* **62(7)**, 1293–1298.

Cheng, G. C. H. & Zussman, J. (1963). The crystal structure of anhydrite ($CaSO_4$). *Acta Crystallographica* **16(8)**, 767–769.

Christensen, A. N. R., Olesen, M., Cerenius, Y. & Jensen, T. R. (2008). Formation and transformation of five different phases in the $CaSO_4$–H_2O system: crystal structure of the subhydrate β-$CaSO_4 + 0{\cdot}5H_2O$ and soluble anhydrite $CaSO_4$. *Chemistry of Materials* **20(6)**, 2124–2132.

Cuss, R. J., Rutter, E. H. & Holloway, R. F. (2003). The application of critical state soil mechanics to the mechanical behaviour of porous sandstones. *International Journal of Rock Mechanics and Mining Science* **40(6)**, 847–862.

de Meer, S. & Spiers, C. J. (1995). Creep of wet gypsum aggregates under hydrostatic loading conditions. *Tectonophysics* **245(3–4)**, 171–183.

de Meer, S. & Spiers, C. J. (1997). Uniaxial compaction creep of wet gypsum aggregates. *Journal of Geophysical Research—Solid Earth* **102(B1)**, 875–891.

Florke, O. W. (1952). *Neues Jahrbuch für Mineralogie* **84**, 189.

Follner, S., Wolter, A., Preusser, A., Indris, S., Silber, C. & Follner, H. (2002). The setting behaviour of α- and β-$CaSO_4.0{\cdot}5\ H_2O$ as a function of crystal structure and morphology. *Crystal Research and Technology* **37(10)**, 1075–1087.

Freyer, D. & Voigt, W. (2003). Crystallization and phase stability of $CaSO_4$ and $CaSO_4$-based salts. *Monatshefte für Chemie* **134(5)**, 693–719.

Fynn, G. W. & Powell, W. F. A. (1979). *The Cutting and Polishing of Electro-optic Materials*. London: Adams Hilger.

Gallitelli, P. (1933). Richerche sul solfato di calcio semidraro e sull'anidrito solubile. *Periodico Mineral Roma* **4**, 1–42.

Hawthorne, F. C. & Ferguson, R. B. (1975). Anhydrous sulphates. II. Refinement of the crystal structure of anhydrite. *Canadian Mineralogist* **13**, 289–292.

Heard, H. C. & Rubey, W. W. (1966). Tectonic implications of gypsum dehydration. *Geological Society of America Bulletin* **77**, 741–760.

Hildyard, R. C., Prior, D. J., Faulkner, D. R. & Mariani, E. (2009*a*). Microstructural analysis of anhydrite rocks from the Triassic Evaporites, Umbria–Marche Apennines, Central Italy: An insight into deformation mechanisms and possible slip systems. *Journal of Structural Geology* **31(1)**, 92–103.

Hildyard, R. C., Prior, D., Mariani, E. & Faulkner, D. R. (2009*b*). Crystallographic Preferred Orientation (CPO) of gypsum measured by Electron Backscatter Diffraction (EBSD). *Journal of Microscopy* **236(3)**, 159–164.

Hubbert, M. K. & Rubey, W. W. (1959). Role of fluid pressure in mechanics of overthrust faulting. 1. Mechanics of fluid-filled porous solids and its application to overthrust faulting. *Geological Society of America Bulletin* **70(2)**, 115–166.

Jiang, Z. X., Li, L. X., Song, Y., Tian, F. H., Zhao, M. J., Wang, H. J. & Zhao, Z. X. (2010). Control of neotectonic movement on hydrocarbon accumulation in the Kuqa Foreland Basin, west China. *Petroleum Science* **7(1)**, 49–58.

Kirfel, A. & Will, G. (1980). Charge density in anhydrite, $CaSO_4$, from X-ray and neutron diffraction measurements. *Acta Crystallography* **B36**, 2881–2890.

Ko, S. C., Olgaard, D. L. & Briegel, U. (1995). The transition from weakening to strengthening in dehydrating gypsum—evolution of excess pore pressures. *Geophysical Research Letters* **22(9)**, 1009–1012.

Kuzel, H. J. & Hauner, M. (1987). Chemical and crystallographic properties of calcium-sulfate hemihydrate and anhydrite-III. *Zement-Kalk-Gips* **40(12)**, 628–632.

Lager, G. A., Armbruster, T., Rotella, F. J., Jorgensen, J. D. & Hinks, D. G. (1984). A crystallographic study of the low-temperature dehydration products of gypsum, CaSO4.2H2O - Hemihydrate CaSO4.0.50H2O, and Gamma-CaSO4. *American Mineralogist* **69(9-10)**, 910–919.

Lasaga, A. C. (1998). *Kinetic Theory in Earth Sciences*. Princeton, NJ: Princeton University Press.

Lloyd, G. E. (1987). Atomic-number and crystallographic contrast images with the SEM—a review of backscattered electron techniques. *Mineralogical Magazine* **51(359)**, 3–19.

McConnell, J. D. C., Astill, D. M. & Hall, P. L. (1987). The pressure-dependence of the dehydration of gypsum to bassanite. *Mineralogical Magazine* **51(361)**, 453–457.

McNamara, D. D. (2009). How do eclogites deform in subduction and collision zones?—An Alpine study. PhD thesis, University of Liverpool, 277 pp.

Meade, C. & Jeanloz, R. (1991). Deep-focus earthquakes and recycling of water into the Earth's mantle. *Science* **252(5002)**, 68–72.

Miller, S. A., van der Zee, W., Olgaard, D. L. & Connolly, J. A. D. (2003). A fluid-pressure feedback model of dehydration reactions: experiments, modelling, and application to subduction zones. *Tectonophysics* **370(1–4)**, 241–251.

Mitchell, T. M. (2007). The fluid flow properties of fault damage zones. PhD thesis, University of Liverpool.

Mitchell, T. M. & Faulkner, D. R. (2008). Experimental measurements of permeability evolution during triaxial compression of initially intact crystalline rocks and implications for fluid flow in fault zones. *Journal of Geophysical Research—Solid Earth* **113(B11)**, 16.

Murrell, S. A. F. & Ismail, I. A. H. (1976). Effect of decomposition of hydrous minerals on mechanical properties of rocks at high pressures and temperatures. *Tectonophysics* **31(3–4)**, 207–258.

Olgaard, D. L., Ko, S.-c. & Wong, T.-f. (1995). Deformation and pore pressure in dehydrating gypsum under transiently drained conditions. *Tectonophysics* **245(3–4)**, 237–248.

Pedersen, B. F. & Semmingsen, D. (1982). Neutron-diffraction refinement of the structure of gypsum, $CaSO_4.22H_2O$. *Acta Crystallographica Section B—Structural Science* **38(Apr)**, 1074–1077.

Prior, D. J., Trimby, P. W., Weber, U. D. & Dingley, D. J. (1996). Orientation contrast imaging of microstructures in rocks using forescatter detectors in the scanning electron microscope. *Mineralogical Magazine* **60(403)**, 859–869.

Raleigh, C. B. & Paterson, M. S. (1965). Experimental deformation of serpentinite and its tectonic implications. *Journal of Geophysical Research* **70(16)**, 3965–3985.

Rutter, E. H., Llana-Fúnez, S. & Brodie, K. H. (2009). Dehydration and deformation of intact cylinders of serpentinite. *Journal of Structural Geology* **31(1)**, 29–43.

Schofield, P. F., Knight, K. S. & Stetton, I. C. (1996). Thermal expansion of gypsum investigated by neutron powder diffraction. *American Mineralogist* **81**, 847–851.

Singh, N. B. & Middendorf, B. (2007). Calcium sulphate hemihydrate hydration leading to gypsum crystallization. *Progress in Crystal Growth and Characterization of Materials* **53(1)**, 57–77.

Stretton, I. (1996). An experimental investigation of the deformation properties of gypsum. PhD thesis, University of Manchester.

Timms, N. E., Li, J. & Reddy, S. M. (2009). Quantitative microstructural characterization of natrojarosite scale formed during high-pressure acid leaching of lateritic nickel ore. *American Mineralogist* **94**, 1111–1119.

Warren, J. K. (2006). *Evaporites: Sediments, Resources, and Hydrocarbons*. Berlin: Springer.

Wong, T. F., Ko, S. C. & Olgaard, D. L. (1997). Generation and maintenance of pore pressure excess in a dehydrating system. 2. Theoretical analysis. *Journal of Geophysical Research—Solid Earth* **102(B1)**, 841–852.

Wood, D. M. (1990). *Soil Behaviour and Critical State Soil Mechanics*. New York: Cambridge University Press.

Yardley, B. W. D. (1989). *An Introduction to Metamorphic Petrology*. Singapore: Addison Wesley Longman.

Zen, E.-A. (1965). Solubility measurements in the system $CaSO_4$–NaCl–H_2O at 35, 50, and 70°C and one atmosphere pressure. *Journal of Petrology* **6**, 124–164.